ACS OMEGA

http://pubs.acs.org/journal/acsodf

Article

Preparation, Characterization, and Photocatalytic Properties of Self-Standing Pure and Cu-Doped TiO_2 Nanobelt Membranes

Hong Zhang* and Baoshun Liu

Cite This: *ACS Omega* 2021, 6, 4534−4541

Read Online

ACCESS | Metrics & More | Article Recommendations

ABSTRACT: A traditional hydrothermal method was modified to synthesize ultra-long sodium titanate nanobelts by simultaneously stirring the solution. The ultra-long sodium titanate nanobelts were converted to hydrogen titanate nanobelts through an ion exchanging way. A method was then used to prepare self-standing flexible large-area membranes; they were then subject to post-annealing at different temperatures to obtain a self-standing TiO_2 nanobelt membrane with a slight decrease in flexibility. Cu-doped TiO_2 membranes were prepared by ion exchanging and post-annealing in the same manner. X-ray diffractions, scanning electron microscopy, field-emission scanning electron microscopy, field-emission transmission electron microscopy, Fourier transform infrared spectrometry, X-ray photoelectron spectroscopy, and UV−vis spectroscopy were used to characterize the samples. Photodegradation of methylene blue (MB) water solutions was used to evaluate the photocatalytic activity. It was seen that the pure sample presented obvious visible-light responding photocatalytic activity, possibly due to the self-sensitization of the MB molecule. The UV-induced photocatalytic activity is higher because of the photoinduced holes and electrons. It was suggested that the Cu dopant induced intra-gap states from electron traps and recombination centers, resulting in the decrease in both of the visible and UV induced photocatalysis.

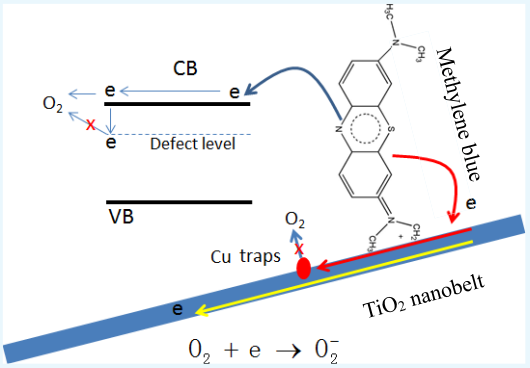

1. INTRODUCTION

TiO_2 still attracts much attention as an important prototype photocatalytic material in these years.[1−7] Photocatalytic effect is its intrinsic property that can be used for pollutant removals and energy generations. Photocatalytic properties of TiO_2 are dependent on the electronic structure, crystalline structure, specific surface area, morphologies, pore structure, and exposed surface facets.[8−11] Engineering TiO_2 materials by altering their morphologies and electronic structures is the main methodologies to increase the photocatalytic activities. Many works were directed to increase the photocatalytic properties through doping, surface modification,[12−15] and nanostructure construction.[16−22] For example, the TiO_2 containing oxygen vacancies or Ti^{3+} has been widely used in enhancing photocatalytic activity and using visible light.[23] Construction of the TiO_2 nanocrystals and nanostructures with highly exposed {001} facets, together integrated with doping and mixing, has also been investigated as an effective ways to increase the photocatalytic activities.[7,24] Grafting the nano-TiO_2 materials with graphene, Au, and other co-catalysts, has also drawn people's interest in photocatalytic H_2 generation and environmental remediation due to the increase in charge transfer.[25,26] For the sample, we combined electrospray and hydrothermal post-treatment to prepare hierarchical TiO_2 materials with high porous volume, which showed high photocatalytic activities.[27−29]

One-dimensional (1-D) nano-TiO_2 materials, including nanotubes, nanorods, and nanofibers, were found to have high photocatalytic activities due to a fast carrier mobility.[30−32] TiO_2 nanotube arrays have been widely used in photocatalysis and solar energy conversion, which were mainly prepared from anodization and hydrothermal methods.[33−35] The 1-D TiO_2 nano-materials can be also prepared through a hydrothermal treatment of layered titanates. As an example, Yang et al. obtained TiO_2(B) nanofibers with a shell of anatase nano-crystals through hydrothermally treating titanates; these materials had high photocatalytic activities because of the special TiO_2(B)/anatase structure.[36] In concentrated NaOH solution, sodium titanate nanotubes, sodium titanate nano-belts, and sodium titanate nanoribbons have been obtained via hydrothermal reactions.[37,38] Sodium titanates have a layered structure; the Na ions locate between $[TiO_6]_8$ interconnected layers. Sodium titanates can be converted to hydrogen titanate through the exchanging of the Na ions with protons; this can

Received: August 12, 2020
Accepted: January 6, 2021
Published: February 8, 2021

https://dx.doi.org/10.1021/acsomega.0c03873
ACS Omega 2021, 6, 4534−4541

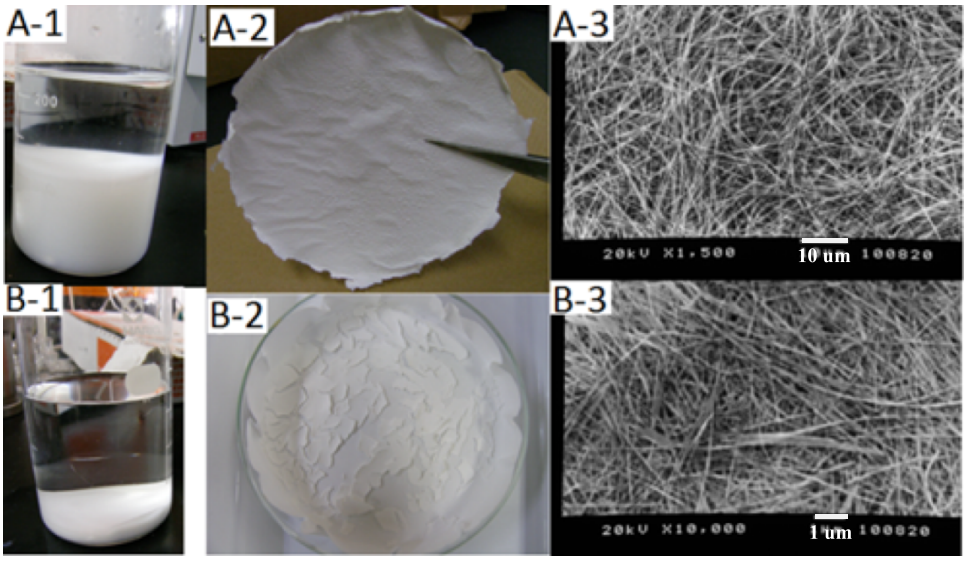

Figure 1. (A-1) Digital picture of the hydrothermal product prepared from the ES materials, dispersed in water. (A-2) Digital picture of the free-standing membrane (ϕ 150 mm) prepared from the H^+-exchanged product. (A-3) SEM image of the membrane composed of entangled ultra-long uniform nanofibers. (B-1) Digital picture of the water dispersion of the hydrothermal product prepared form the commercial p25 powder. (B-2) Digital picture of the cracked membrane. (B-3) SEM image of the membrane composed of nanofibers.

be converted to 1-D TiO_2 nano-materials by annealing. Both the titanate and the 1-D TiO_2 materials are active in removing pollutants under illumination of UV and visible lights.[39,40] In the present research, a modified hydrothermal reaction was first used to fabricate ultra-long hydrogen titanate nanobelts, which were then used to prepare large-area flexible titanate membranes. The titanate membranes were then changed to TiO_2 membranes by annealing at different temperatures, and the photocatalytic activities of them were studied. The Cu ions were also doped in the TiO_2 membranes; it was seen that the photocatalytic activities decreased possibly because the Cu dopants might form recombination centers and electron traps. As compared to powder photocatalysts, the self-standing membranes do not need additional supports and can be easily separated from the reaction solution. Therefore, they cannot lead to the secondary particle pollution and can be easily recycled and reactivated.

2. EXPERIMENTAL SECTION

2.1. Synthesis of TiO_2 Nanobelt Membranes. TiO_2 amorphous materials were first prepared by an electrospray method according to previous studies.[27−29] Then, 0.3 g electro-sprayed (ES) powder was hydrothermally treated in 50 mL 10 M NaOH aqueous solution in a Teflon-lined stainless-steel autoclave at 180 and 200 °C for 24 h. The hydrothermal solutions were continuously stirred during the hydrothermal reactions. Afterward, the products were cleaned by deionized water several times until the pH was 7, which were then immersed in 0.01 M HCl aqueous solution for 24 h at room temperature to exchange Na^+ ions with H^+ ions. After then, the products were washed repeatedly with deionized water until the pH was neutral. The as-cleaned materials were then dispersed in ethanol and were then spread on a filter paper (ϕ 150 mm) placed upon the bottom of a glass container. The ethanol was slowly removed by a glass pipette, and the material was dried at ∼100 °C for about 1 h to obtain the final product. A piece of membrane can then be peeled off from the filter paper. The as-prepared membranes were annealed at 400, 500, 600, 700, 800, and 900 °C for 2 h, respectively, to obtain TiO_2 membranes. Instead of the ES materials, the commercial P25 TiO_2 powder was also used as the raw material to prepare membranes according to the same procedure.

For the preparation of the Cu-doped TiO_2 paper, the H^+-exchanged hydrothermal products were immersed in 500 mL of 0.01, 0.05, and 0.1 mol L^{-1} $CuCl_2$ water solution at room temperature for 24 h to exchange partial H^+ ions with Cu^{2+} ions. The Cu^{2+}-exchanged products were then washed repeatedly with deionized water to remove physically adsorbed Cu^{2+} ions. The Cu-doped membranes were obtained according to the same procedure. Lastly, the Cu-doped titanate membranes were annealed at 500, 600, 700, 800, and 900 °C, respectively.

2.2. Characterization. Powder X-ray diffractions (XRD) were used to determine the crystalline phases of the membranes using an RINT 1500 diffractometer (made in Japan) with the Cu Kα radiation being used as the X-ray source. The morphologies were observed using a scanning electron microscope (SEM, SEM-5400, JEOL, Japan) with an accelerated voltage of 20 kV and a field emission scanning electron microscope (FE-SEM, S-4800, Hitachi, Japan) with an accelerated voltage of 10 kV. High-resolution field emission transmission electron microscopy (FE-TEM, EM002BF, Japan) was used to observe the sample morphologies with an accelerated voltage of 160 kV. Ultraviolet−visible (UV−vis) absorption spectra were recorded using a UV−vis spectrophotometer (UV-2450, Shimadzu, Japan) in a wavelength range from 300 to 800 nm. The XPS survey spectrum and core-level spectra of Ti2p, Cu2p, Na1s, and O1s were recorded using X-ray photoelectron spectroscopy (VG Multilab2000X) with an X-ray source working with the Al Kα radiation and using the binding energy (284.6 eV) of C1s electrons as the energy reference. The measurement step size is 0.05 eV. Fourier transformation infrared (FT-IR) absorption spectra of the membranes annealed at different temperatures were obtained

https://dx.doi.org/10.1021/acsomega.0c03873
ACS Omega 2021, 6, 4534−4541

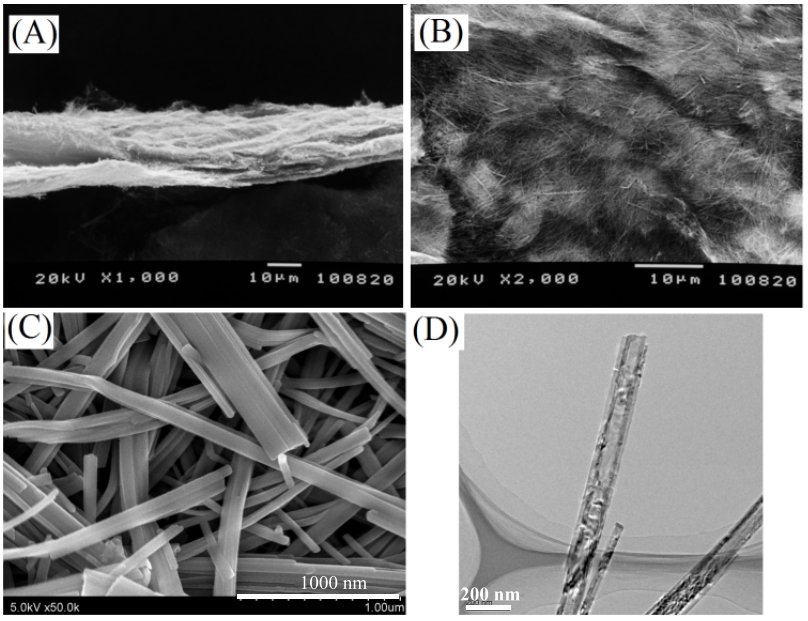

Figure 2. (A) Cross-sectional SEM image of the membrane prepared from the ES materials. (B) Low-magnified SEM image of the membrane prepared from the commercial P25 powders. (C) High-resolution FE-SEM image of the membrane prepared from the ES materials. (D) TEM image of the 1-D nanobelts.

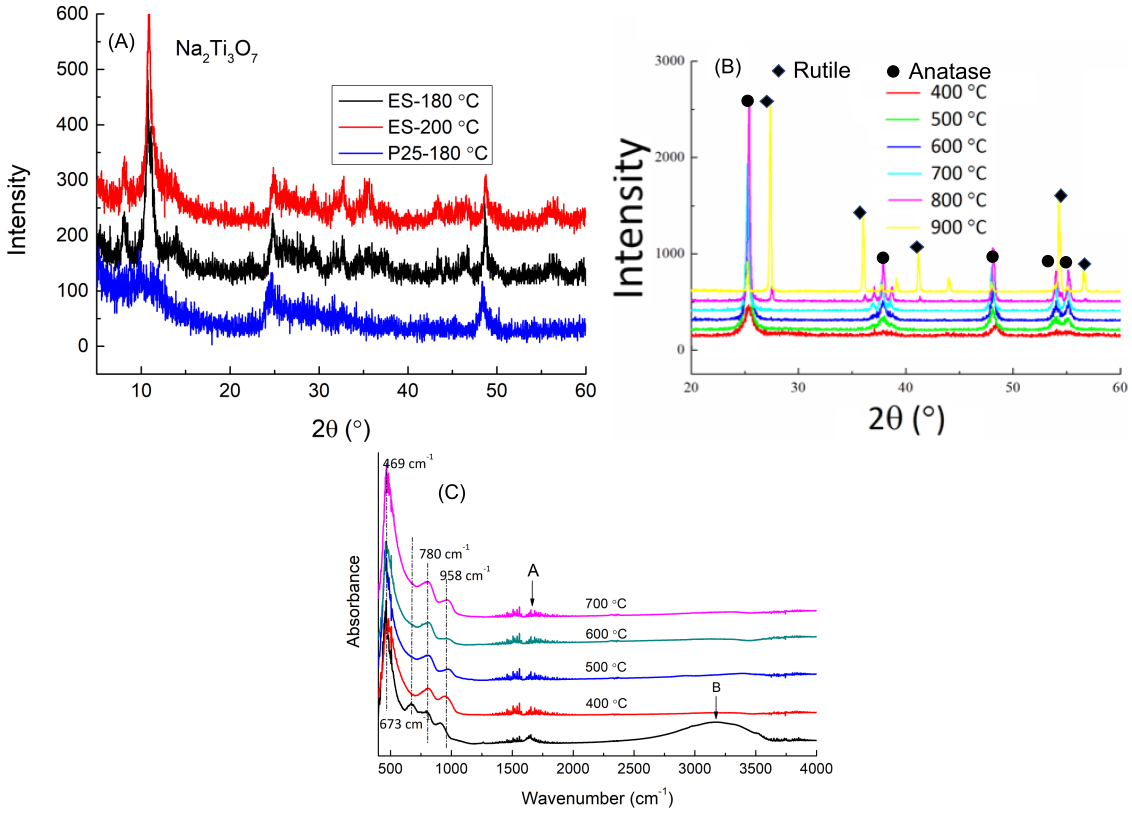

Figure 3. (A) XRD patterns of the hydrothermal products prepared from the ES and the commercial P25 materials. (B) XRD patterns of the membranes after post-annealing. (C) FTIR spectra of the H^+-exchanged membrane and the membranes after post-annealing at different temperatures.

on an FT-IR spectrometer (FT/IR-6100, JASCO, Japan) from 450 to 4000 cm^{-1}.

2.3. Photocatalytic Activity Measurement. A small piece of the TiO_2 membrane (~ 0.04 g) was used to degrade the methylene blue (MB) aqueous solution (1.0×10^{-5} mol L^{-1}) under visible light and UV light illuminations, respectively. The TiO_2 membrane was placed in a ϕ 50 mm glass container, with the 20 mL MB water solution being added. For the photocatalytic reactions under visible light illumination, two 15 W daylight lamps, equipped with a 420

https://dx.doi.org/10.1021/acsomega.0c03873
ACS Omega 2021, 6, 4534−4541

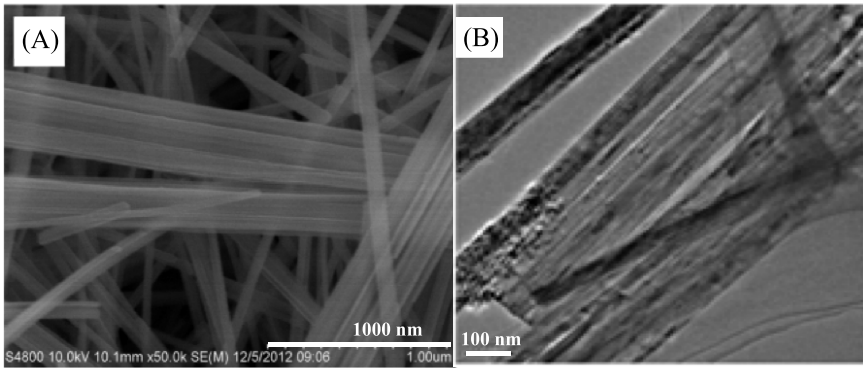

Figure 4. (A) FE-SEM image of the hydrogen titanate membrane subjected to 2 h post-annealing at 500 °C. (B) Corresponding TEM image.

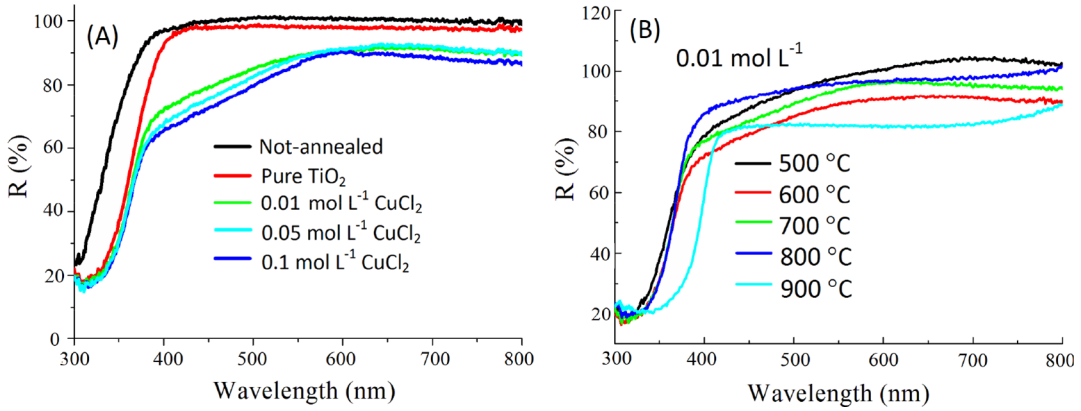

Figure 5. (A) UV−Vis diffusion absorptions of the hydrogen titanate membrane, pure anatase TiO_2 membrane, and Cu-doped anatase TiO_2 membranes. (B) UV−Vis diffusion absorptions of Cu-doped TiO_2 membranes prepared through the calcination of titanate membranes at different temperatures.

nm short-wavelength cutting filter to remove UV light, were used. Four 15 W UV 365 nm fluorescent lights were used to conduct the UV-induced photocatalysis. The light intensity of UV light was ~3 mW/cm^2. The concentrations of reacted MB water solutions were recorded with a UV−visible spectrometer (UV-1601, Japan) after a certain time interval. The photocatalytic activities were evaluated from the decrease of the MB absorbance at 660 nm during the photocatalytic reactions.

3. RESULTS AND DISCUSSION

Figure 1A-1 shows the digital picture of the hydrothermally reacted product. The product presents a flocky form that almost filled the half of a beaker (200 mL). Figure 1A-2 shows the digital picture of the as-prepared pre-annealed membrane with a diameter of ϕ 150 mm and a weight of ca. 0.2 g. This membrane was flexible and could be bent repeatedly several times without damage, so it can be fabricated as various shapes. The SEM image (Figure 1A-3) shows that the membrane is composed of ultra-long (>100 μm) uniform 1-D nanofibers, which entangled together to form a large-area membrane. Figure 1B-1 shows the digital picture of the hydrothermal product prepared from the commercial P25 TiO_2; the product becomes precipitates on the beaker bottom, which is greatly different from Figure 1A-1. We cannot obtain a complete membrane, but some small fragments (Figure 1B-2), although the product also consists of 1-D nanofibers (Figure 1B-3).

Figure 2A shows the cross-sectional SEM image of the membrane prepared from the ES materials. It is seen that the thickness of the membrane is ca. 20 μm. Figure 2B shows the SEM image of the cracked segments prepared from the commercial P25. Although the nanofibers also entangled together, they broke into small pieces after drying. This indicates that the flexibility of the nanofibers should be lower than that prepared from the ES materials, so a complete membrane cannot be obtained. The FE-SEM image (Figure 2C) shows that the 1-D nanofibers in the membrane prepared from ES materials are in the form of nanobelts. The single nanobelt has a width of ~50 nm. Some of them compact together layer by layer to form polymerized nanobelts, finally presenting in nanofiber morphology. The TEM image (Figure 2D) also shows the 1-D nanobelt morphology. The nanobelts cannot be obtained if the hydrothermal solutions were not stirred during reactions. Because the ES materials used in the hydrothermal reactions are amorphous TiO_2-polymer (PVP) aggregates, stirring was necessary to break the TiO_2-polymer aggregates to react with the highly concentrated NaOH water solutions in order to obtain the nanobelt morphology.

Figure 3A shows the XRD patterns of the as-prepared hydrothermal products prepared from the ES materials at 180 and 200 °C, respectively; the XRD pattern of the sample prepared from the commercial P25 powder at 180 °C is also shown. It is seen that the crystalline phase is $Na_2Ti_3O_7$. Clearly, the products prepared from the ES materials have better crystallinity than that prepared from the P25 powder, which prefer to grow along the [200] (2θ:11°) direction. Because of the better crystallinity of the $Na_2Ti_3O_7$ nanobelts, they can have stronger mechanical intensity and are longer to form nanobelt membranes. Figure 3B shows the XRD patterns

https://dx.doi.org/10.1021/acsomega.0c03873
ACS Omega 2021, 6, 4534−4541

of the membranes annealed at the temperatures from 400 to 900 °C. It is seen that the crystalline phase is converted to anatase TiO_2 when the temperature is below 800 °C. If the temperature is higher than 900 °C, then the titanate was changed to rutile TiO_2. The higher transition temperature of anatase-to-rutile (A-R) transformation is due to the suppression of A-R transition in the course of calcination by the residual Na^+ ions in the TiO_2 nanobelt membrane as revealed by the XPS analysis below. The residual Na^+ ions should limit the interface diffusion that is necessary for phase transformation. Figure 3C shows the FT-IR spectra of the H^+-exchanged nanobelt membrane, and the membranes annealed at 400, 500, 600, and 700 °C. The IR absorption bands labeled as A and B are ascribed to the physically absorbed water and chemically bonded hydroxyl groups (OH^-) in hydrogen titanates, respectively. After calcination, the chemically bonded OH^- disappears due to phase transition to anatase TiO_2. The IR absorption peak at 469 cm^{-1} is from the Ti−O−Ti vibrations of the anatase lattice. For the titanate nanobelts, there are three IR peaks at 673, 780, and 958 cm^{-1}, arising from the Ti−O−Ti vibrations in the Ti−O layer. After calcination, the peak at 673 cm^{-1} disappeared due to the phase transition.

Figure 4A shows the FE-SEM image of the nanobelt membrane after 2 h of annealing at 500 °C. It is seen that the annealing process did not destroy the 1-D nanobelt morphology. Figure 4B shows the corresponding TEM image, which also shows the form of nanobelts and several of nanobelts fused together. Therefore, the post-annealing does not change the morphology of the nanobelts although it is transformed to anatase TiO_2, so the sample still presents the shape of the membrane. The flexibility decreases because of the increase in fragility.

Figure 5A shows the UV−vis absorption spectra of the hydrogen titanate membrane, pure TiO_2 nanobelt membrane annealed at 600 °C, and Cu-doped TiO_2 membranes annealed at 600 °C prepared by the ion exchanging with different concentrations of $CuCl_2$ solutions. The titanate membrane (labeled as "not annealed", black line) has no visible light absorption; the absorption edge is located near 360 nm. The absorption edge of the pure TiO_2 membrane shifts to 420 nm; this agrees well with the XRD analysis that the titanate phase was transformed to anatase TiO_2. The introduction of Cu ions in TiO_2 generates obvious absorption in the visible region from 400 to 600 nm; this increases with the increase in $CuCl_2$ solution concentrations. It is seen that the Cu doping almost does not affect the absorption edge of the TiO_2 membrane; this means that the Cu dopants form the gap states and do not affect the conduction band (CB) and valence band (VB) of TiO_2. The effect of annealed temperature on the UV−vis absorptions was also studied, as shown in Figure 5B. The annealing below 800 °C did not change the absorption edge of Cu-doped TiO_2 samples, indicating that the crystalline phase of anatase is unchanged. When the annealing temperature increased to 900 °C, the absorption edge shows an obvious redshift due to the anatase-to-rutile transition, in good accordance with the XRD analysis. It is also seen that the Cu doping leads to a wide absorption from 400 to 800 nm in the rutile phase, different from the anatase case.

XPS was employed to explore the chemical states of surface elements of the Cu-doped TiO_2 membrane prepared from the 0.1 mol L^{-1} $CuCl_2$ solution and the post-annealing at 600 °C. Figure 6 shows the XPS survey spectra of the Cu-doped

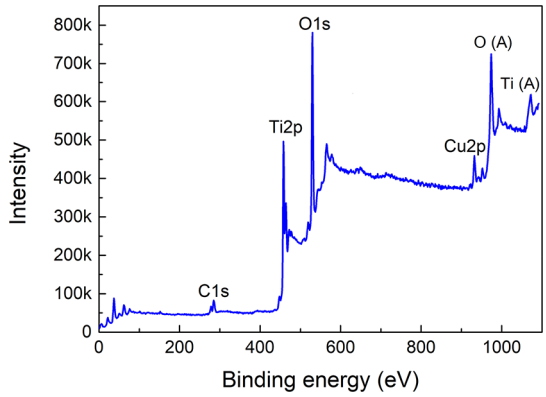

Figure 6. XPS survey spectrum of the Cu-doped TiO_2 membrane.

sample, which shows that it contains C, Ti, O, and Cu elements. The C element comes from the oil contaminants in the XPS measurement. The peak near 1070 eV might be ascribed to Na1s or Ti Auger peaks. As no Na Auger peak around 470 eV was detected, this peak is attributed to the Ti (A) peak. This result indicates that almost all of Na ions in the samples can be removed by the ion exchanging, in accordance with the XRD analysis. The peak around 970 eV is ascribed to the O Auger peak. Figure 7 shows the core-level XPS spectra of the Cu2p, O1s, and Ti2p, respectively. The Cu2p3/2 was fitted with two Lorentz−Gaussian peaks, showing the presence of Cu^0/Cu^+ and Cu^{2+} species.[13,41−43] The Cu^{2+} species are also indicated by the satellite peak in the spectrum. The atomic ratio of Cu^0/Cu^+ and Cu^{2+} is about 3:1, so Cu dopants mainly exist in the Cu^0/Cu^+ state. Figure 7B shows that the O1s spectrum can be also fitted with two peaks, showing the presence of hydroxyl groups in addition to the lattice oxygens. Figure 7C shows the Ti2p XPS peaks at 463.9 and 458.2 eV that can be well fitted with two Lorentz−Gaussian peaks. The 5.7 eV splitting of spin-orbital coupling between them indicate the +4 valence of Ti ions. The presence of residual Na^+ ions might increase the A-R transition temperatures. Combining the UV−vis analysis and XPS analysis, we suggested that the Cu ions should enter the TiO_2 lattice. Corresponding oxygen impurities should also be generated in the sample in order to keep electric neutrality. The Cu species and oxygen impurities may lead to the exponential tail of the Cu-induced absorption, as shown in Figure 5A.

Figure 8 shows the change of normalized MB concentrations in the dark, under visible light illumination, and under UV light illumination. The pure TiO_2 and the Cu-doped membranes, which were obtained by annealing at 600 °C, were used as the photocatalysts. After the dark absorption reached equilibrium, the visible light was first turned on. It is seen that the pure TiO_2 membrane shows an obvious photocatalytic activity, which tends to disappear after Cu doping. This result seems to contradict with the common knowledge that the visible light activity should increase because the Cu-doped TiO_2 absorbs visible light. Afterward, the visible light was turned off, and the UV light was turned on. It is seen that the UV-induced photocatalysis becomes faster than the visible-induced photocatalysis. The Cu doping also greatly decreases the UV-induced photocatalytic activity.

Figure 9A shows the normalized concentrations of the MB solutions in the dark and under visible light illumination for the TiO_2 membranes obtained by annealing at different temperatures. It is seen that the dark absorption amount of the MB on

https://dx.doi.org/10.1021/acsomega.0c03873
ACS Omega 2021, 6, 4534−4541

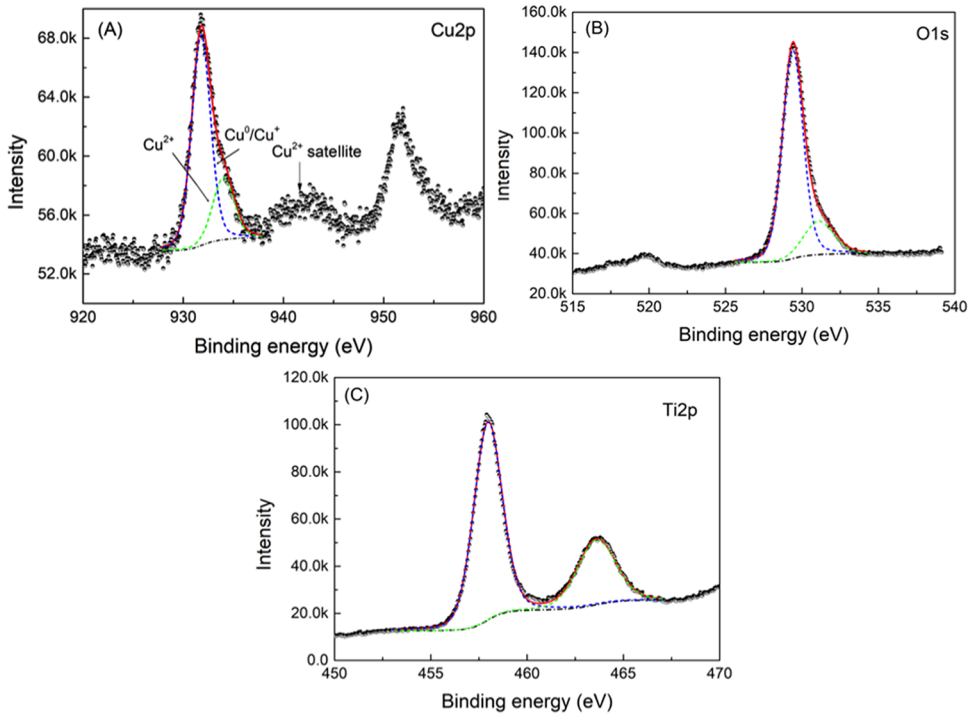

Figure 7. (A) Cu2p core-level XPS spectrum. (B) O1s core-level XPS spectrum. (C) Ti2p core-level XPS spectrum

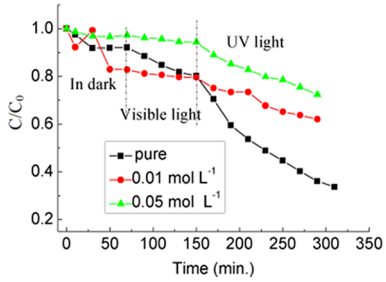

Figure 8. Dependences of normalized MB concentrations (C/C_0) on time in the dark and during the photocatalytic reactions over the pure TiO_2 membrane and Cu-doped TiO_2 membranes prepared from 0.01 and 0.05 mol L^{-1} $CuCl_2$ water solutions

the TiO_2 membranes increases with the increase in annealing temperatures. Nearly 70% of MB can be adsorbed by the sample prepared by annealing at 900 °C. Under visible light illumination, all of the samples show the photocatalytic activities. The photocatalytic activities of the anatase samples (annealed below 800 °C) are slightly better than that of the rutile sample (annealed at 900 °C); this is consistent with the common knowledge that the anatase has higher activity than the rutile TiO_2.[44] Because the TiO_2 membranes do not absorb the light below 420 nm, it is suggested that the visible-induced photocatalysis may be caused by the self-sensitization of the MB molecule adsorbed on the TiO_2 surface. Figure 9B shows the dark adsorption and the photocatalytic degradation of MB solutions under visible light illumination by the Cu-doped TiO_2 membrane prepared by the post-annealing at 900 °C. The crystalline phase of TiO_2 is rutile. Independent on the doped Cu amount, it is seen the Cu-doped membranes also have strong dark absorption. They do not show visible activity, the same as the anatase cases.

Figure 10 shows the proposed mechanism of self-sensitized photocatalysis and the effect of Cu dopants. Under visible light illumination, the electrons can be excited from the highest occupied molecular orbitals (HOMOs) of the MB molecules to their lowest unoccupied molecular orbitals (LUMOs). The electrons in the LUMOs can transfer to the CB of the TiO_2,

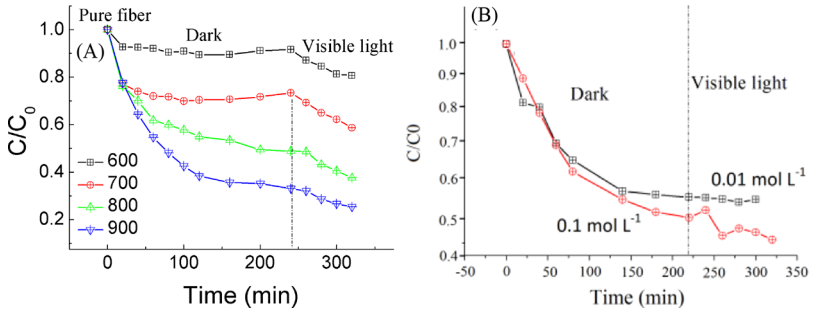

Figure 9. (A) Time dependence of the normalized concentrations (C/C_0) of the MB solutions in the dark and under visible light illumination for the pure TiO_2 membranes prepared by post-annealing at different temperatures. (B) Time dependence of the C/C_0 of the MB solutions in the dark and under visible light illumination for the Cu-doped TiO_2 membranes prepared from the 0.01 and 0.1 mol L^{-1} $CuCl_2$ solutions.

https://dx.doi.org/10.1021/acsomega.0c03873
ACS Omega 2021, 6, 4534−4541

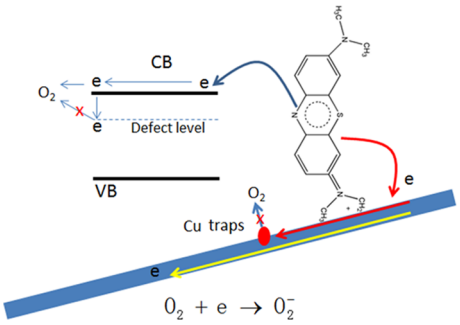

Figure 10. Proposed mechanism of self-sensitized photocatalysis and the photocatalytic effect prohibited by the Cu dopants.

and they can then transport along the 1-D TiO_2 materials. The pure TiO_2 membranes are well crystalline and contain less electrons traps, so the electrons from the MB molecule can transfer to the O_2 molecule and cause the formation of super oxygen free radicals (O_2^-). The O_2^- is an important reactive oxidative species (ROS) that can induce the formation of H_2O_2 and $^{\cdot}OH$ (hydroxyl free groups). These ROSs lead to the MB photodegradation under visible light illumination. The UV−vis absorptions indicate that the Cu dopants should mainly form deep gap states (defect levels) in the forbidden gap of the TiO_2. The deep gap states can trap the electrons from the CB of TiO_2 materials, which then become immobile and need a long time to be detrapped to the CB, so the transfer of the electrons to O_2 is limited and the photocatalysis is thus stopped. The mechanism of the UV light-induced photocatalytic effect is different, which arises from the generation of photoinduced holes and electrons in the CB and the VB of the TiO_2 samples. The photocatalytic results also indicate that the Cu dopants mainly form the recombination centers for the photoinduced holes and electrons, which results in the decrease in photocatalytic activities.

4. CONCLUSIONS

A facile method was used to fabricate ultra-long nanobelt sodium titanates, which were then converted to hydrogen titanates by H^+ exchanging. The ultra-long hydrogen titanates were used to construct self-standing large-area membranes. The TiO_2 nanobelt membranes were obtained by the post-annealing of the hydrogen titanate membranes. Cu-doped TiO_2 membranes were also prepared by exchanging the H^+ in hydrogen titanate with Cu^{2+} ions before membrane construction. It was seen that the TiO_2 membrane showed a high temperature for A-R phase transition due to the existence of residual Na^+ ions. The valence state of Cu dopants includes both Cu^+ and Cu^{2+}, which causes obvious visible absorption ranging from 400 to 600 nm for anatase and 400 to 800 nm for rutile. The UV−visible absorptions show that Cu dopants created gap states in the TiO_2. In additional to the UV-induced photocatalytic effect, the pure TiO_2 membranes also showed the self-sensitized photocatalytic effect for photodegrading the MB under visible light illumination. Independent on the Cu doping, the TiO_2 membrane also showed good ability for the MB dark adsorption. It was seen that the Cu dopants reduced the photocatalytic activities for both UV and visible light illuminations, possibly because they formed electron traps and recombination centers.

AUTHOR INFORMATION

Corresponding Author

Hong Zhang − *Transportation institute, Inner Mongolia University, Hohhot, Inner Mongolia 010070, China*; Phone: +86-0471-4996820; Email: zhanghong3537@126.com

Author

Baoshun Liu − *State Key Laboratory of Silicate Materials for Architectures, Wuhan University of Technology, Wuhan, Hubei Province 430070, China*; orcid.org/0000-0001-5564-3685

Complete contact information is available at: https://pubs.acs.org/10.1021/acsomega.0c03873

Notes

The authors declare no competing financial interest.

ACKNOWLEDGMENTS

B.L. thanks the National Natural Science Foundation of China (no. 51772230) and National Key Research and Development Project (no. 2017YFE0192600).

REFERENCES

(1) Chen, B.; Meng, Y.; Sha, J.; Zhong, C.; Hu, W.; Zhao, N. Preparation of MoS_2/TiO_2 Based Nanocomposites for Photocatalysis and Rechargeable Batteries: Progress, Challenges, and Perspective. *Nanoscale* **2018**, *10*, 34−68.

(2) Liu, B.; Zhao, X.; Yu, J.; Parkin, I. P.; Fujishima, A.; Nakata, K. Intrinsic intermediate gap states of TiO_2 materials and their roles in charge carrier kinetics. *J. Photochem. Photobiol., C* **2019**, *39*, 1−57.

(3) Liu, B.; Wu, H.; Parkin, I. P. Gaseous Photocatalytic Oxidation of Formic Acid over TiO_2: A Comparison between the Charge Carrier Transfer and Light-Assisted Mars−van Krevelen Pathways. *J. Phys. Chem. C* **2019**, *123*, 22261−22272.

(4) Bian, Z.; Zhu, J.; Cao, F.; Huo, Y.; Lu, Y.; Li, H. Solvothermal Synthesis of Well-defined TiO_2 Mesoporous Nanotubes with Enhanced Photocatalytic Activity. *Chem. Commun.* **2010**, *46*, 8451−8453.

(5) Nair, A. S.; Shengyuan, Y.; Peining, Z.; Ramakrishna, S. Rice Grain-shaped TiO_2 Mesostructures by Electrospinning for Dye-sensitized Solar Cells. *Chem. Commun.* **2010**, *46*, 7421−7423.

(6) Tang, J.; Durrant, J. R.; Klug, D. R. Mechanism of Photocatalytic Water Splitting in TiO_2. Reaction of Water with Photoholes, Importance of Charge Carrier Dynamics, and Evidence for Four-Hole Chemistry. *J. Am. Chem. Soc.* **2008**, *130*, 13885−13891.

(7) Ong, W.-J.; Tan, L.-L.; Chai, S.-P.; Yong, S.-T.; Mohamed, A. R. Highly Reactive {001} Facets of TiO_2-based Composites: Synthesis, Formation Mechanism and Characterization. *Nanoscale* **2014**, *6*, 1946−2008.

(8) Leung, D. Y. C.; Fu, X.; Wang, C.; Ni, M.; Leung, M. K. H.; Wang, X.; Fu, X. Hydrogen Production over Titania-based Photocatalysts. *ChemSusChem* **2010**, *3*, 681−694.

(9) Wang, J.; Liu, B.; Nakata, K. Effects of Crystallinity,{001}/{101} Ratio, and Au Decoration on the Photocatalytic Activity of Anatase TiO_2 Crystals. *Chin. J. Catal.* **2019**, *40*, 403−412.

(10) Li, L.; Gibson, E. A.; Qin, P.; Boschloo, G.; Gorlov, M.; Hagfeldt, A.; Sun, L. Double-layered NiO Photocathodes for p-type DSSCs with Record IPCE. *Adv. Mater.* **2010**, *22*, 1759−1762.

(11) Liu, B.; Yan, L.; Wang, J. Liquid N_2 Quenching Induced Oxygen Defects and Surface Distortion in TiO_2 and the Effect on the Photocatalysis of Methylene Blue and Acetone. *Appl. Surf. Sci.* **2019**, *494*, 266−274.

(12) Yu, H.; Irie, H.; Shimodaira, Y.; Hosogi, Y.; Kuroda, Y.; Miyauchi, M.; Hashimoto, K. An Efficient Visible-Light-Sensitive

https://dx.doi.org/10.1021/acsomega.0c03873
ACS Omega 2021, 6, 4534−4541

Fe(III)-Grafted TiO_2 Photocatalyst. *J. Phys. Chem. C* **2010**, *114*, 16481−16487.
(13) Liu, M.; Qiu, X.; Miyauchi, M.; Hashimoto, K. Cu(II) Oxide Amorphous Nanoclusters Grafted Ti^{3+} Self-Doped TiO_2: An Efficient Visible Light Photocatalyst. *Chem. Mater.* **2011**, *23*, 5282−5286.
(14) Liu, B.; Wang, X.; Cai, G.; Wen, L.; Song, Y.; Zhao, X. Low Temperature Fabrication of V-doped TiO2 Nanoparticles, Structure and Photocatalytic Studies. *J. Hazard. Mater.* **2009**, *169*, 1112−1118.
(15) Wen, L.; Liu, B.; Zhao, X.; Nakata, K.; Murakami, T.; Fujishima, A. Synthesis, Characterization, and Photocatalysis of Fe-doped: a Combined Experimental and Theoretical Study. *Int. J. Photoenergy* **2012**, 368750.
(16) Zhu, X.; Xu, H.; Yao, Y.; Liu, H.; Wang, J.; Pu, Y.; Feng, W.; Chen, S. Effects of Ag^0-Modification and Fe^{3+}-doping on the Structural, Optical and Photocatalytic Properties of TiO^2. *RSC Adv.* **2019**, *9*, 40003−40012.
(17) Guo, Q.; Zhou, C.; Ma, Z.; Yang, X. Fundamentals of TiO_2 Photocatalysis: Concepts, Mechanisms, and Challenges. *Adv. Mater.* **2019**, *31*, 1901997.
(18) Li, M.; Song, W.; Zeng, L.; Zeng, D.; Xie, C.; Yang, O. Mechanistic Study of N−H-and H−N-codoping of a TiO_2 Photocatalyst for Efficient Degradation of Benzene under Visible Light. *RSC Adv.* **2020**, *10*, 2757−2766.
(19) Sboui, M.; Bouattour, S.; Gruttadauria, M.; Liotta, L. F.; La Parola, V.; Boufi, S. Hybrid paper−TiO_2 Coupled with a Cu_2O Heterojunction: an Efficient Photocatalyst under Sun-light Irradiation. *RSC Adv.* **2016**, *6*, 86918−86929.
(20) Chen, D.; Huang, F.; Cheng, Y.-B.; Caruso, R. A. Mesoporous Anatase TiO_2 Beads with High Surface Areas and Controllable Pore Sizes: A Superior Candidate for High-Performance Dye-Sensitized Solar Cells. *Adv. Mater.* **2009**, *21*, 2206−2210.
(21) Yang, S.-C.; Yang, D.-J.; Kim, J.; Hong, J.-M.; Kim, H.-G.; Kim, I.-D.; Lee, H. Hollow TiO_2 Hemispheres Obtained by Colloidal Templating for Application in Dye-Sensitized Solar Cells. *Adv. Mater.* **2008**, *20*, 1059−1064.
(22) Wang, J.; Zhou, Y.; Hu, Y.; O'Hayre, R.; Shao, Z. Facile Synthesis of Nanocrystalline TiO_2 Mesoporous Microspheres for Lithium-Ion Batteries. *J. Phys. Chem. C* **2011**, *115*, 2529−2536.
(23) Pan, X.; Yang, M.-Q.; Fu, X.; Zhang, N.; Xu, Y.-J. Defective TiO_2 with Oxygen Vacancies: Synthesis, Properties and Photocatalytic Applications. *Nanoscale* **2013**, *5*, 3601−3614.
(24) Ong, W.-J.; Tan, L.-L.; Chai, S.-P.; Yong, S.-Y.; Mohamed, A. R. Facet-dependent Photocatalytic Properties of TiO_2-based Composites for Energy Conversion and Environmental Remediation. *ChemSusChem* **2014**, *7*, 690−719.
(25) Liu, L.; Liu, Z.; Liu, A.; Gu, X.; Ge, C.; Gao, F.; Dong, L. Engineering the TiO_2−Graphene Interface to Enhance Photocatalytic H_2 Production. *ChemSusChem* **2014**, *7*, 618−626.
(26) Yao, Q.; Wang, C.; Wang, H.; Yan, H.; Lu, J. Revisiting the Au Particle Size Effect on TiO_2-Coated Au/TiO_2 Catalysts in CO Oxidation Reaction. *J. Phys. Chem. C* **2016**, *120*, 9174−9183.
(27) Liu, B.; Zhao, X.; Nakata, K.; Fujishima, A. Construction of Hierarchical Titanium Dioxide Nanomaterials by Tuning the Structure of Polyvinylpyrrolidone−titanium Butoxide Complexes from 2-to 3-dimensional. *J. Mater. Chem. A* **2013**, *1*, 4993−5000.
(28) Liu, B.; Nakata, K.; Sakai, M.; Saito, H.; Ochiai, T.; Murakami, T.; Takagi, K.; Fujishima, A. Mesoporous TiO_2 Core−Shell Spheres Composed of Nanocrystals with Exposed High-Energy Facets: Facile Synthesis and Formation Mechanism. *Langmuir* **2011**, *27*, 8500−8508.
(29) Liu, B.; Nakata, K.; Sakai, M.; Saito, H.; Ochiai, T.; Murakami, T.; Takagi, K.; Fujishima, A. Hierarchical TiO_2 Spherical Nanostructures with Tunable Pore Size, Pore Volume, and Specific Surface Area: Facile Preparation and High-photocatalytic Performance. *Catal. Sci. Technol.* **2012**, *2*, 1933−1939.
(30) Shao, F.; Sun, J.; Gao, L.; Yang, S.; Luo, J. Growth of Various TiO_2 Nanostructures for Dye-Sensitized Solar Cells. *J. Phys. Chem. C* **2011**, *115*, 1819−1823.
(31) Shi, J.; Sun, C.; Starr, M. B.; Wang, X. Growth of Titanium Dioxide Nanorods in 3D-Confined Spaces. *Nano Lett.* **2011**, *11*, 624−631.
(32) Wang, G.; Wang, H.; Ling, Y.; Tang, Y.; Yang, X.; Fitzmorris, R. C.; Wang, C.; Zhang, J. Z.; Li, Y. Hydrogen-Treated TiO_2 Nanowire Arrays for Photoelectrochemical Water Splitting. *Nano Lett.* **2011**, *11*, 3026−3033.
(33) Ge, M.; Li, Q.; Cao, C.; Huang, J.; Li, S.; Zhang, S.; Chen, Z.; Zhang, K.; al-Deyab, S. S.; Lai, Y. One-dimensional TiO_2 Nanotube Photocatalysts for Solar Water Splitting. *Adv. Sci.* **2019**, 1600152.
(34) Kontos, A. I.; Likodimos, V.; Stergiopoulos, T.; Tsoukleris, D. S.; Falaras, P.; Rabias, I.; Papavassiliou, G.; Kim, D.; Kunze, J.; Schmuki, P. Self-Organized Anodic TiO_2 Nanotube Arrays Functionalized by Iron Oxide Nanoparticles. *Chem. Mater.* **2009**, *21*, 662−672.
(35) Liu, B.; Aydil, E. S. Growth of Oriented Single-Crystalline Rutile TiO_2 Nanorods on Transparent Conducting Substrates for Dye-Sensitized Solar Cells. *J. Am. Chem. Soc.* **2009**, *131*, 3985−3990.
(36) Yang, D.; Liu, H.; Zheng, Z.; Yuan, Y.; Zhao, J. C.; Waclawik, E. R.; Ke, X.; Zhu, H. An Efficient Photocatalyst Structure: TiO_2(B) Nanofibers with a Shell of Anatase Nanocrystals. *J. Am. Chem. Soc.* **2009**, *131*, 17885−17893.
(37) Nakahira, A.; Kubo, T.; Numako, C. TiO_2-Derived Titanate Nanotubes by Hydrothermal Process with Acid Treatments and Their Microstructural Evaluation. *ACS Appl. Mater. Interfaces* **2010**, *2*, 2611−2616.
(38) Tang, Y.; Yang, L.; Chen, J.; Qiu, Z. Facile Fabrication of Hierarchical Hollow Microspheres Assembled by Titanate Nanotubes. *Langmuir* **2010**, *26*, 10111−10114.
(39) Zhang, Y.; Xing, Z.; Liu, X.; Li, Z.; Wu, X.; Jiang, J.; Li, M.; Zhu, Q.; Zhou, W. Ti^{3+} Self-Doped Blue TiO_2(B) Single-Crystalline Nanorods for Efficient Solar-Driven Photocatalytic Performance. *ACS Appl. Mater. Interfaces* **2016**, *8*, 26851−26859.
(40) Liu, B.; Khare, A.; Aydil, E. S. TiO_2−B/Anatase Core−Shell Heterojunction Nanowires for Photocatalysis. *ACS Appl. Mater. Interfaces* **2011**, *3*, 4444−4450.
(41) Qiu, X.; Miyauchi, M.; Sunada, K.; Minoshima, M.; Liu, M.; Lu, Y.; Li, D.; Shimodaira, Y.; Hosogi, Y.; Kuroda, Y.; Hashimoto, K. Hybrid Cu_xO/TiO_2 Nanocomposites As Risk-Reduction Materials in Indoor Environments. *ACS Nano* **2012**, *6*, 1609−1618.
(42) Poulston, S.; Parlett, P. M.; Stone, P.; Bowker, M. Surface Oxidation and Reduction of CuO and Cu_2O Studied Using XPS and XAES. *Surf. Interface Anal.* **1996**, *24*, 811−820.
(43) Biesinger, M. C.; Lau, L. W. M.; Gerson, A. R.; Smart, R. S. C. Resolving surface chemical states in XPS analysis of first row transition metals, oxides and hydroxides: Sc, Ti, V, Cu and Zn. *Appl. Surf. Sci.* **2010**, *257*, 887−898.
(44) Yamada, Y.; Kanemitsu, Y. Determination of Electron and Hole Lifetimes of Rutile and Anatase TiO_2 Single Crystals. *Appl. Phys. Lett.* **2012**, *101*, 133907.

https://dx.doi.org/10.1021/acsomega.0c03873
ACS Omega 2021, 6, 4534−4541